Relativistic magnetic reconnection in laser laboratory for testing an emission mechanism of hard-state black hole system

K. F. F. Law,[1,2] Y. Abe,[1] A. Morace,[1] Y. Arikawa,[1] S. Sakata,[1,3] S. Lee,[1] K. Matsuo,[1,4] H. Morita,[1] Y. Ochiai,[1] C. Liu,[1] A. Yogo,[1,5] K. Okamoto,[1] D. Golovin,[1] M. Ehret,[6,7] T. Ozaki,[8] M. Nakai,[1] Y. Sentoku,[1] J. J. Santos,[6] E. d'Humières,[6] Ph. Korneev,[9,10] and S. Fujioka[1,*]

[1]*Institute of Laser Engineering, Osaka University, 2-6 Yamadaoka, Suita, Osaka 565-0871, Japan*
[2]*Department of Earth and Planetary Science, The University of Tokyo, 7-3-1 Hongo, Bunkyo-ku, Tokyo 113-0033, Japan*
[3]*Administration and Technology Center for Science and Engineering, Technology Management Division, Waseda University, 3-4-1 Okubo, Shinjyuku-ku, Tokyo 169-8555, Japan*
[4]*Center for Energy Research, University of California, San Diego, La Jolla, California 92093-0417, USA*
[5]*PRESTO, Japan Science and Technology Agency, 4-1-8 Honmachi, Kawaguchi, Saitama 332-0012, Japan*
[6]*Université de Bordeaux, CNRS, CEA, CELIA (Centre Lasers Intenses et Applications), UMR 5107, Talence, France*
[7]*Institut für Kernphysik, Technische Universität Darmstadt, D-64289 Darmstadt, Germany*
[8]*National Institute for Fusion Science, National Institutes of Natural Sciences, 322-6 Oroshi-Cho, Toki, Gifu 509-5292, Japan*
[9]*National Research Nuclear University MEPhI (Moscow Engineering Physics Institute), 31 Kashirskoe shosse, Moscow, 115409, Russian Federation*
[10]*P. N. Lebedev Physics Institute, Russian Academy of Sciences, 53 Leninskiy Prospekt, Moscow, 119991, Russian Federation*

(Received 29 August 2019; revised 6 July 2020; accepted 28 July 2020; published 3 September 2020)

Magnetic reconnection in a relativistic electron magnetization regime was observed in a laboratory plasma produced by a high-intensity, large energy, picoseconds laser pulse. Magnetic reconnection conditions realized with a laser-driven several kilotesla magnetic field is comparable to that in the accretion disk corona of black hole systems, i.e., Cygnus X-1. We observed particle energy distributions of reconnection outflow jets, which possess a power-law component in a high-energy range. The hardness of the observed spectra could explain the hard-state x-ray emission from accreting black hole systems.

DOI: 10.1103/PhysRevE.102.033202

I. INTRODUCTION

Magnetic reconnection is a process whereby magnetic field lines in opposite directions cancel each other, resulting in the rearrangement of magnetic field topology associated with the conversion of magnetic field energy into the kinetic energy (KE) of energetic particles [1]. This process occurs in magnetized astrophysical plasmas, e.g., those in the solar corona, Earth's magnetosphere, and active galactic nuclei. The magnetic reconnection accounts for various phenomena, e.g., solar flares [2], energetic particle acceleration [3], and powering of photon emission [4]. In this work, we report the experimental demonstration of magnetic reconnection in the relativistic electron magnetization domain, along with the observation of power-law distributed outflow particles, both electrons and protons.

In this work, by irradiation of an intense laser on a "microcoil," a relativistic and highly magnetized plasma was produced and magnetic reconnection occurred with maximum magnetic field $2.09^{+2.10}_{-0.13}$ kT. In the downstream outflow direction, a nonthermal component was observed in the high-energy part of both electron and proton energy distributions, with a significantly harder power-law slope for the electron high-energy distribution ($p_e = 1.535 \pm 0.015$); here p_e is the index of the power-law distribution for electrons, represented as $f(E) \propto E^{p_e}$. This energy distribution is similar to that predicted by the electron injection model [5] that was proposed to explain the hard x-ray emission tail from galactic x-ray sources with the same order of magnetization, e.g., Cygnus X-1. The experimental result tested that magnetic reconnection can build a hard electron population in the emitting region of a galactic x-ray source under electron magnetization condition of $\sigma_e \sim 100$.

Magnetic reconnection occurs widely in the universe [1], making it very natural to be studied based on telescopic observations of accessible astronomical plasmas. There are not many cases where we can observe directly the magnetic reconnection, and most of the phenomena occur too distant to perform direct observations. For further study on the fundamental physical processes involved in magnetic reconnection, laboratory experiments have been attempted using different approaches, mainly categorized into magnetic confined plasmas or laser-produced plasmas. The former includes studies in spherical torus devices [6], MRX [7], VTF [8], and more recent facilities such as TREX [9].

Several schemes were investigated with laser-produced plasmas to study magnetic reconnection: Zhong *et al.* simulated a solar flare x-ray loop-top source by producing a pair of expanding plasma bubbles around the focus spots of an

*sfujioka@ile.osaka-u.ac.jp

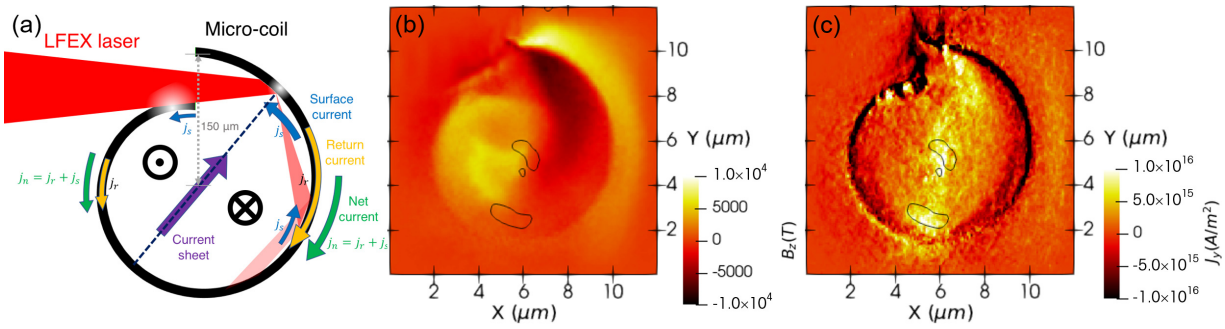

FIG. 1. (a) Bidirectional current is produced by laser irradiation on two separate positions of the microcoil. (b) The 3D PIC simulation results with $\frac{1}{30}$ downsized microcoil shows that antiparallel magnetic field structure B_z (component perpendicular to the cross section) formed inside the single microcoil. This field reconnect with each other within the boundary. The boundary of the region with electron dissipation measure [27] $D_e > 0.5 v_A B_0 j_0$ is plotted by black solid lines, indicates magnetic reconnection sites. (c) Current sheet J_y in same simulation, plotted together with the boundary of $D_e > 0.5 v_A B_0 j_0$. v_{A0}, B_0, and j_0 are the Alfvén velocity, magnetic field, and current density in simulation, respectively, as in the previous study [27].

intense laser, with a frozen-in magnetic field generated by the Biermann battery effect [10]. Pei *et al.* observed low-β ($\beta \sim 0.016$) magnetic reconnection using a magnetic field generated by laser-driven double coil target at the GEKKO XII laser facility [11], β is defined as a value of plasma thermal pressure divided by magnetic pressure. The experiments above were performed with "long-pulse" (pulse duration of the order of nanoseconds) lasers having intensities of 10^{14}–10^{16} W/cm^2. Raymond *et al.* demonstrated magnetic reconnection through a pair of plasma bubbles produced by relativistic intensity and shorter-pulse laser ($I > 10^{18}$ W/cm^2). $\beta \sim 50$ was achieved in experiments performed on OMEGA-EP and HERCULES [12].

II. MAGNETIC RECONNECTION BY MICROCOIL

Figure 1 shows the experimental schemes used in this magnetic reconnection study. The magnetic reconnection experiment was performed using a "microcoil," which was first proposed by Korneev *et al.* to generate sub-gigagauss magnetic field by laser-induced electron current [13]. A high-intensity and short pulse laser enters the microcoil and it propagates along the curved surface by multiple reflections at grazing incidence [14], a current of accelerated relativistic electrons j_s is established along the microcoil surface [15]. A return current of bulk electrons j_r sets up quasi-instantaneously to neutralize j_s [13]. The net current $j_n = j_r + j_s$ always points away from the laser-plasma interaction position, at which an electron vacancy is generated due to the electron ejection by the direct laser acceleration. Instead of one directional j_n found in the original paper [13], we generated bidirectional j_n in a single microcoil by simultaneous laser irradiation at two separated positions. This was achieved using a laser beam with a sufficiently large focus spot size comparable to the entrance slit width of the microcoil. A portion of a laser beam entered inside of the microcoil and multiple reflections occurred, while the remaining part of the laser beam irradiated the edge of the entrance slit, resulting in an additional j_n pointing in the opposite direction.

A pair of kilotesla, antiparallel magnetic fields B_0 were generated by these bidirectional currents as shown in Fig. 1(b). As a typical consequence of laser-plasma interaction, the plasma expands from the coil inner wall inwardly in radial direction and converges at the center of the microcoil with the frozen-in antiparallel magnetic field. The evolution of magnetic field topology is shown in Fig. 2, by three snapshots in three-dimensional particle-in-cell (3D PIC) simulations representing the topology before, during, and after the magnetic reconnection, respectively. As signature of magnetic reconnection, quadrupole magnetic field configuration developed by the Hall effect, from the decoupling between electron flow and ion flow by multifluid effect, is observed around the reconnection site in Fig. 2(e).

The experiment was performed on the petawatt laser facility LFEX, with four-beam capability of maximum energy of 500 J per beam at a wavelength of 1.053 nm [16]. In this experiment, two beams of LFEX were operated. One beam of LFEX (pulse duration: 1.2 ps, average energy: 330 J) was focused on the microcoil with a focus spot having a full width at half-maximum (FWHM) of 40 μm, corresponding to a peak laser intensity of 1.4×10^{19} W/cm^2. The other beam was irradiated on a thin foil to acceleration ion via target normal sheath acceleration mechanism [17], for magnetic field characterization which is described in the next section. The microcoil was fabricated from 10-μm-thick Cu foil, with a radius of 150 μm and a length of $l = 500$ μm along its rotational axis. Stacks of radiochromic film (RCF) were placed in both the radial and axial directions in order to record the spatial distributions of protons deflected by the magnetic field, those directed along the current sheet, and those in the outflow jets, as shown in Fig. 3, Within a part of the laser shots, energy distributions of protons and electrons in the jets were recorded by a Thomson parabola spectrometer (TPS) [18] and an electron spectrometer (ESM) was placed at the both sides, instead of the corresponding RCF stacks.

III. MAGNETIC FIELD CHARACTERIZATION

Before observation of the magnetic reconnection outflow, the magnetic field geometry and amplitude were characterized experimentally. The magnetic field configuration inside the microcoil was characterized experimentally with proton deflectometry [19], which is applicable to kilotesla magnetic field in sub-mm scale [20,21]. In order to generate the proton beam, another beam of LFEX was focused on an Al foil to

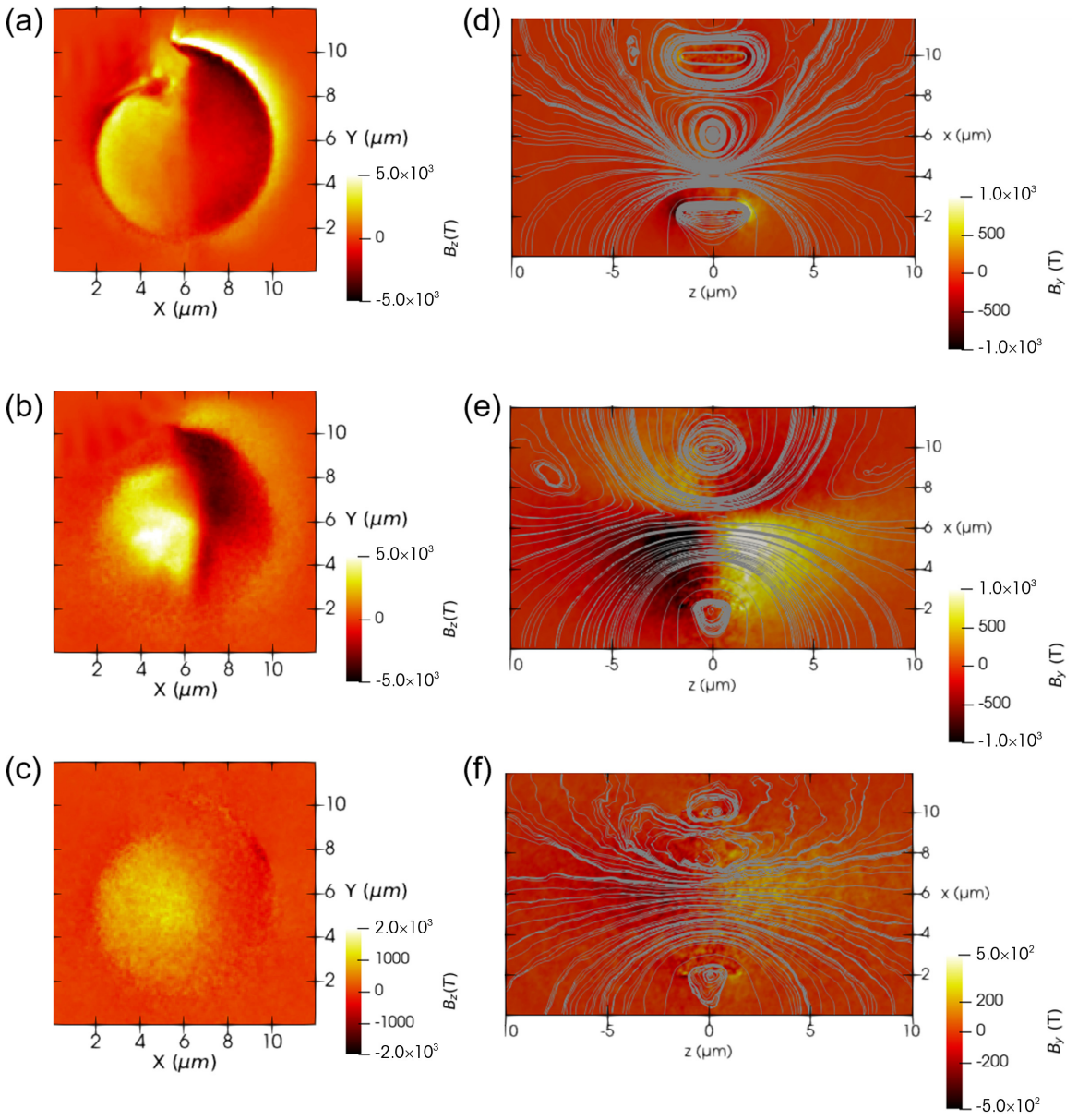

FIG. 2. Magnetic field topology extracted from PIC simulation, at snapshots of before, during, and after the magnetic reconnection. (a)–(c) Reconnection magnetic field component B_z on x-y plane at $z = 0$. (d)–(f) Streamline plot of magnetic field on x-z plane at $y = 6.5$ μm. Color map shows the out-of-plane component B_y.

accelerate proton by the target normal sheath acceleration mechanism [17], with adjustable time difference Δt from the microcoil irradiation, which is provided by the capability of LFEX interbeam synchronization. The probing proton beam was deflected in a magnetic field, its deflected pattern was then recorded with a RCF stack placed as surrounding the microcoil, positioned 3 cm from the microcoil. The setup for proton deflectometry is shown in Fig. 4. An RCF stack consists of a number of RCF layers and various aluminum filters between different layers. The signal detected by the RCFs depends solely on the particle energy deposition within the thin (7–15 μm) active layer. Therefore, the spatial pattern of the signal on a single RCF can be reasonably assumed to be dominated by protons carrying KE that correspond to the Bragg peak on the active layer. The value of KE corresponding to each RCF layer is calculated by the PHITSMonte Carlo particle transport simulation code [22]. From multiple layers of RCF in a single stack, every layer with analyzable proton pattern probes the magnetic field at a different time, intrinsically by the different time of flight of protons carrying different KE. Time of flight is $t_{\text{flight}} = l/v_p$ for $l = 3$ mm, which is the distance between the proton generation site and the microcoil. The LFEX interbeam time difference between laser irradiation of two targets is $\delta t = 69$ ps in order to capture the magnetic field generated during and after the laser irradiation. The unaffected proton beam pattern and deflected proton beam pattern are shown in Fig. 5.

In order to determine the magnetic field from deflected probe proton pattern, the magnetic field geometry must be assumed. Here, we constructed a current model assuming that the magnetic field is generated by current flow along the microcoil and the current sheet (indicated by green and purple

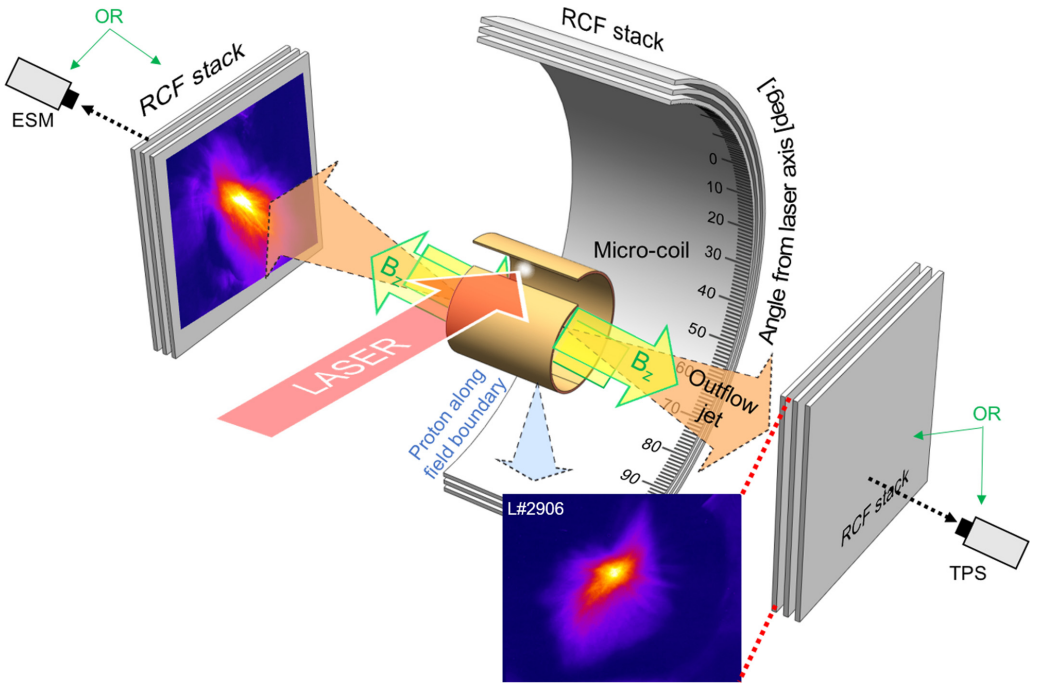

FIG. 3. The curved RCF stack surrounding the microcoil was used to measure the proton beam along the field boundary and also to detect spatial profiles of proton beams deflected by the magnetic field in the microcoil. A pair of RCF stacks was used to detect the angular distribution of the protons in the outflow jets. The two proton patterns, which appeared to be symmetric, were obtained from the same laser shot. In the selected shots, electron energy spectrometer (ESM) and Thomson parabola ion energy analyzer (TPS) were placed instead of the two RCF stacks.

arrows, respectively, in Fig. 1). In this model, the microcoil is modeled as the analytically defined shape $r(\theta) = r_0[1 + (\delta r/r_0)(\theta/2\pi)]$, with $r_0 = 100$ μm, $\delta r = 50$ μm. Schematic diagram of the current model is shown in Fig. 6(a). The current density is assumed to be uniform along the z direction,

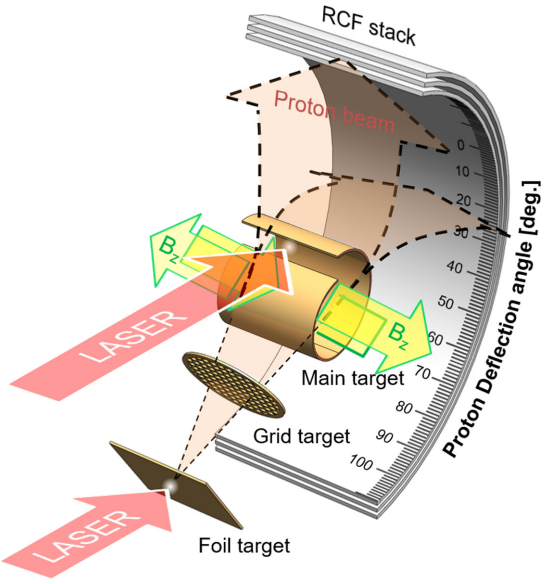

FIG. 4. Experimental setup for magnetic field characterization. A grid is placed between the proton source and the microcoil for analysis purposes. Angular distribution of the deflected proton is measured by the curved RCF stack.

and the extension length is assumed to be the same as the length of the microcoil (500 μm). As shown in Fig. 6(b), the current flow along the microcoil is approximated as varying linearly along the θ direction with two different current density values at the ends of the microcoil, which is observed in the PIC simulation described in the later section. The current sheet, also acting as the boundary between the antiparallel magnetic field, is modeled at the center of the microcoil.

In this current model, the orientation of the current sheet is one of the parameters to be experimentally determined, by measuring the direction of proton beam accelerated in the current sheet direction. In the previous study [13], the formation of initial current flow between the antiparallel magnetic field regions was identified as a consequence of fast electrons deflected by the generated magnetic field. In our numerical simulation, a similar current structure is observed at the center of the microcoil. While this confinement decouples electrons from ions, an electric field that points into the current flow is formed. The corresponding component of the electric field is plotted as Fig. 7, which clearly shows this feature around the current sheet. As a result of this effect, a fraction of protons (fewer than the number of electrons) are guided along the current flow, so that the net current is dominated by electron flow. Through this mechanism, protons are guided along the magnetic field boundary and escape from the microcoil as a proton beam along the direction parallel to this boundary. In the experiment, this proton beam is detected by an RCF stack in a shot without the probing proton beam. The proton flux has a single peak at 145° from the incidence laser direction,

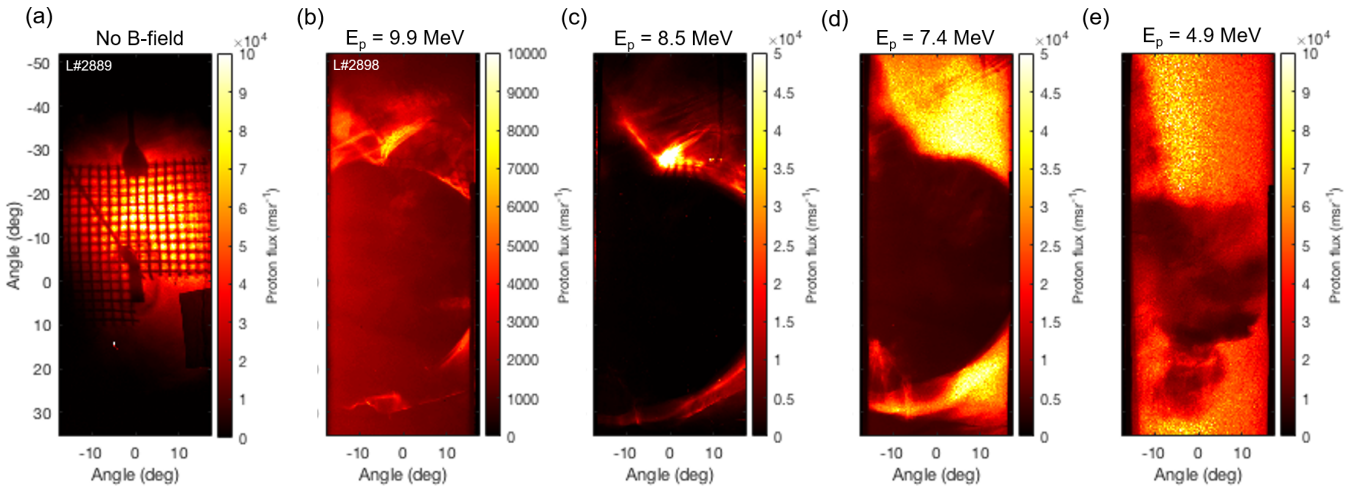

FIG. 5. Proton beam spatial pattern obtained in the experiment. Proton pattern (a) without magnetic field deflection and (b)–(e) under magnetic field deflection are shown, which probed the magnetic field generated by the microcoil. Four proton patterns in the same measurement shot are shown in descending order of proton KE, which is equivalent to showing the probed magnetic field from the earlier one to the later one. In all measurements, a grid is placed between the proton source and microcoil.

which is shown in Fig. 8. As the result, we approximated the magnetic field configuration with a boundary aligned along this direction in our magnetic field model.

The current density value at the two microcoil sides is another important parameter to be determined. From observation of PIC simulation results, at the intersection between the current sheet and microcoil, the tangential component of the current density changes its sign where its magnitude falls to zero. Based on these constraints and assumptions, the modeled current sheet is pointing to the experimentally determined direction mentioned above, and the current amplitudes are determined as I_0 and $-0.66I_0$. In the magnetic field model, the current density in the current sheet is taken as constant $I_{\text{sheet}} = cI_0$, with c a free parameter to be determined.

With this magnetic field model depending only on the value of I_0 and c, classical Runge-Kutta scheme Monte Carlo simulations are performed on particle tracing in the proton probing beam under the Lorentz force by the magnetic field. The magnetic field profile is calculated from the above current model by 3D magnetostatic code RADIA [23]. The divergence angle of source protons is obtained from experimental measurement of the undeflected proton beam. In simulation, source protons are assumed to be monoenergetic because of the Bragg peak property of proton energy deposition on a given RCF active layer, as discussed above. Here we take the RCF layer corresponding to 9.9 MeV, the highest detected proton KE within the RCF layers, as an example case of our analysis. We performed a parameter scan on I_0 and current sheet parameter c. Some examples of the synthetic proton patterns are shown in Fig. 9, and we found that the measured proton pattern can only be reproduced when $0.1 < c < 0.2$. Within this range of c, $I_0 = 2.14$–2.41 MA best fit the

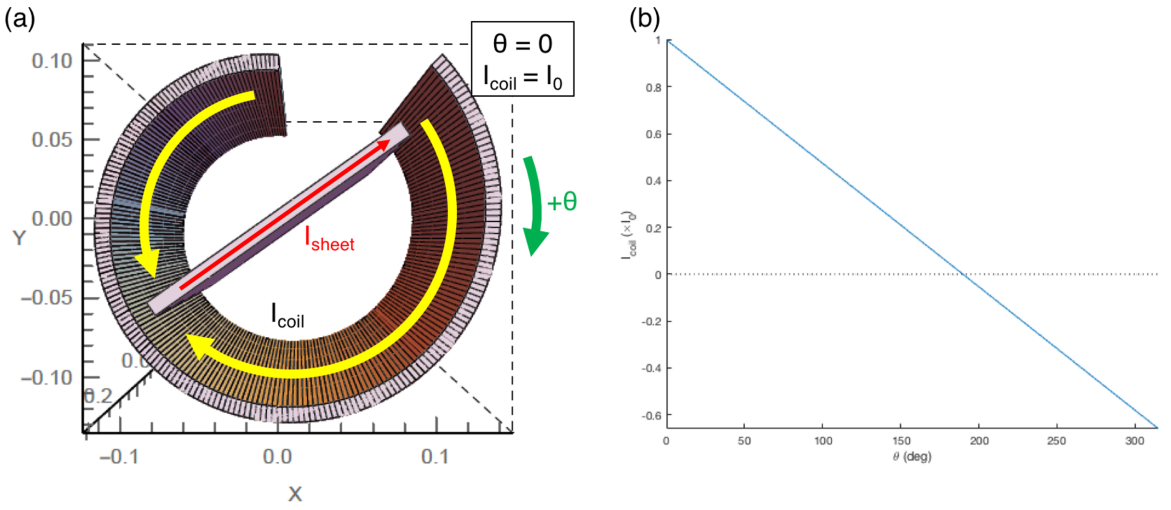

FIG. 6. Current model constructed based on experimental results. (a) Schematic of current model, consisted of current flow in θ direction along the microcoil I_{coil} and current sheet I_{sheet} across the microcoil. Positive value of I_{coil} corresponds to clockwise current flow in diagram. (b) Distribution of I_{coil} along θ direction. $\theta = 0$ correspond to one end of I_{coil}, which is the incident laser focus spot in the experiment.

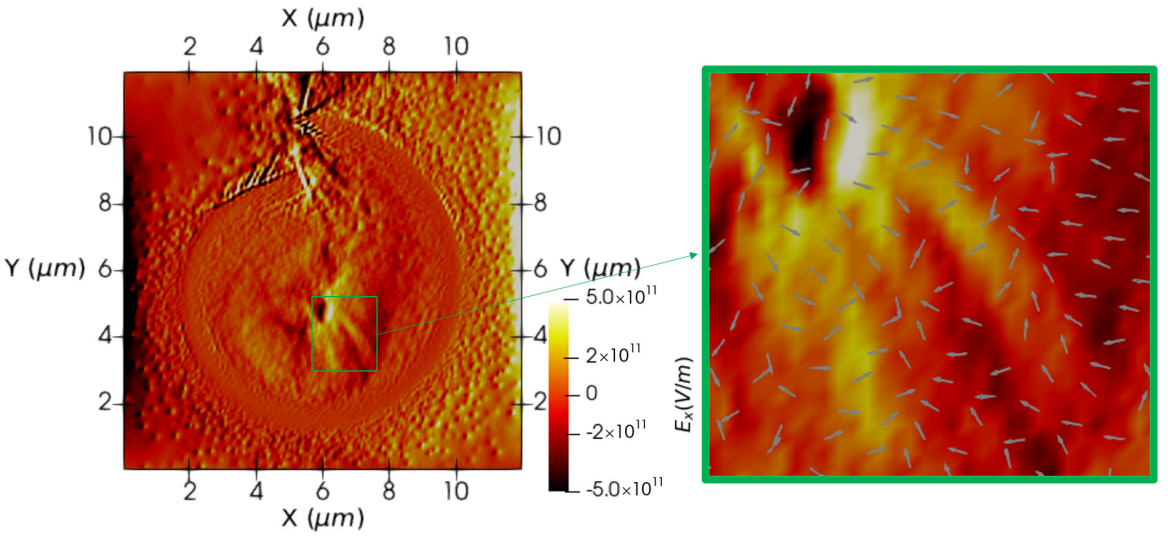

FIG. 7. Electric field E_x at $z = 0$. Vectors of electric field x-y component are plotted in region of green box, showed how the electric field contributed on the proton flow along the reconnection field boundary.

experimental result [Fig. 5(b)], and $B_{\max} = 2.09 \pm 0.13$ kT is determined with uncertainty due to the unknown I_{sheet}. The two earliest data points are estimated to have uncertainty of 50% and 10% to be underestimated, accounting for the effect of the probing protons that have already entered or approached close to the microcoil when the magnetic field is generated. Accounting for this, $B_{\max} = 2.09^{+2.10}_{-0.13}$ kT at $t = 0.9 \pm 0.65$ ps, with $t = 0$ being the peak timing of the incident laser pulse. By analysis on each RCF layer, considering the temporal uncertainties from the RCF energy uncertainty and the time of flight of proton inside the microcoil interior, the measurements of magnetic field until $t = 29.3$ ps are plotted in Fig. 10. The magnetic field value decreased to 0.54 ± 0.03 kT at 29.3 ps after laser irradiation. Solely by this measurement, this drop of magnetic field may be accounted by dissipation through magnetic reconnection or other mechanisms, for example, being carried out by the plasma expansion. In the following section, the results of reconnection

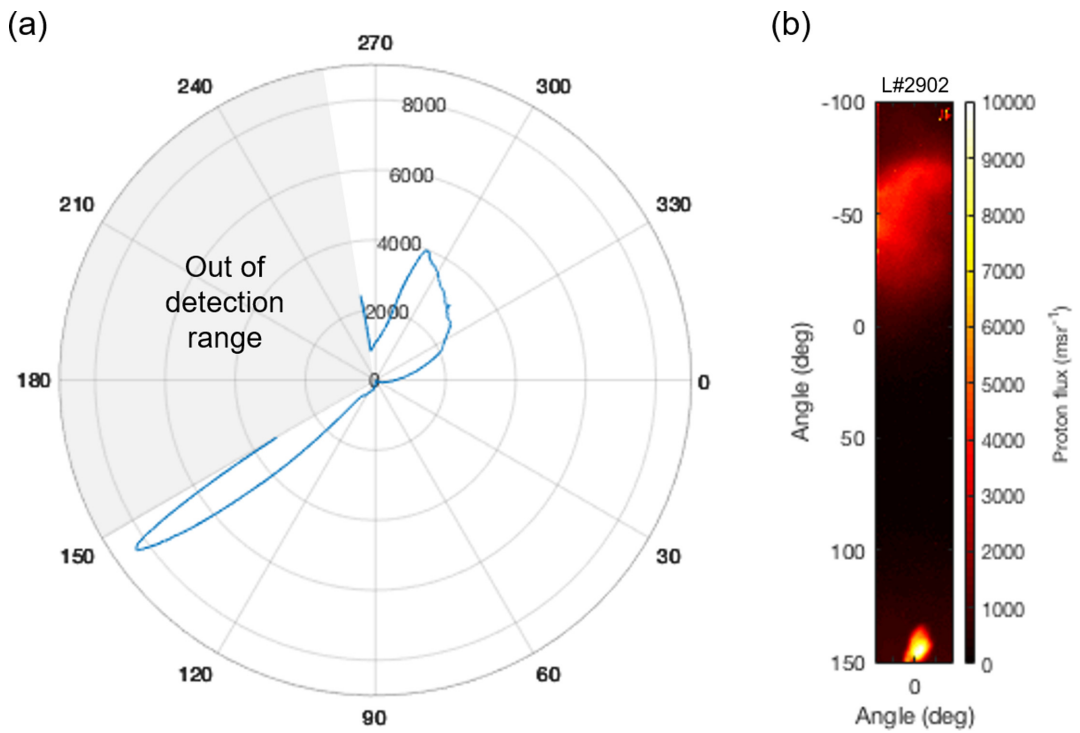

FIG. 8. Distribution of protons detected in the radial direction of the microcoil. (a) Polar plot of average RCF signal from −5° to 5°. (b) RCF signal obtained in experiment. The highly collimated signal observed at 145° is a typical signature of proton beam. The direction of this proton beam provided information of the magnetic field geometry inside the microcoil. No probing protons produced from the auxiliary target were used in this laser shot.

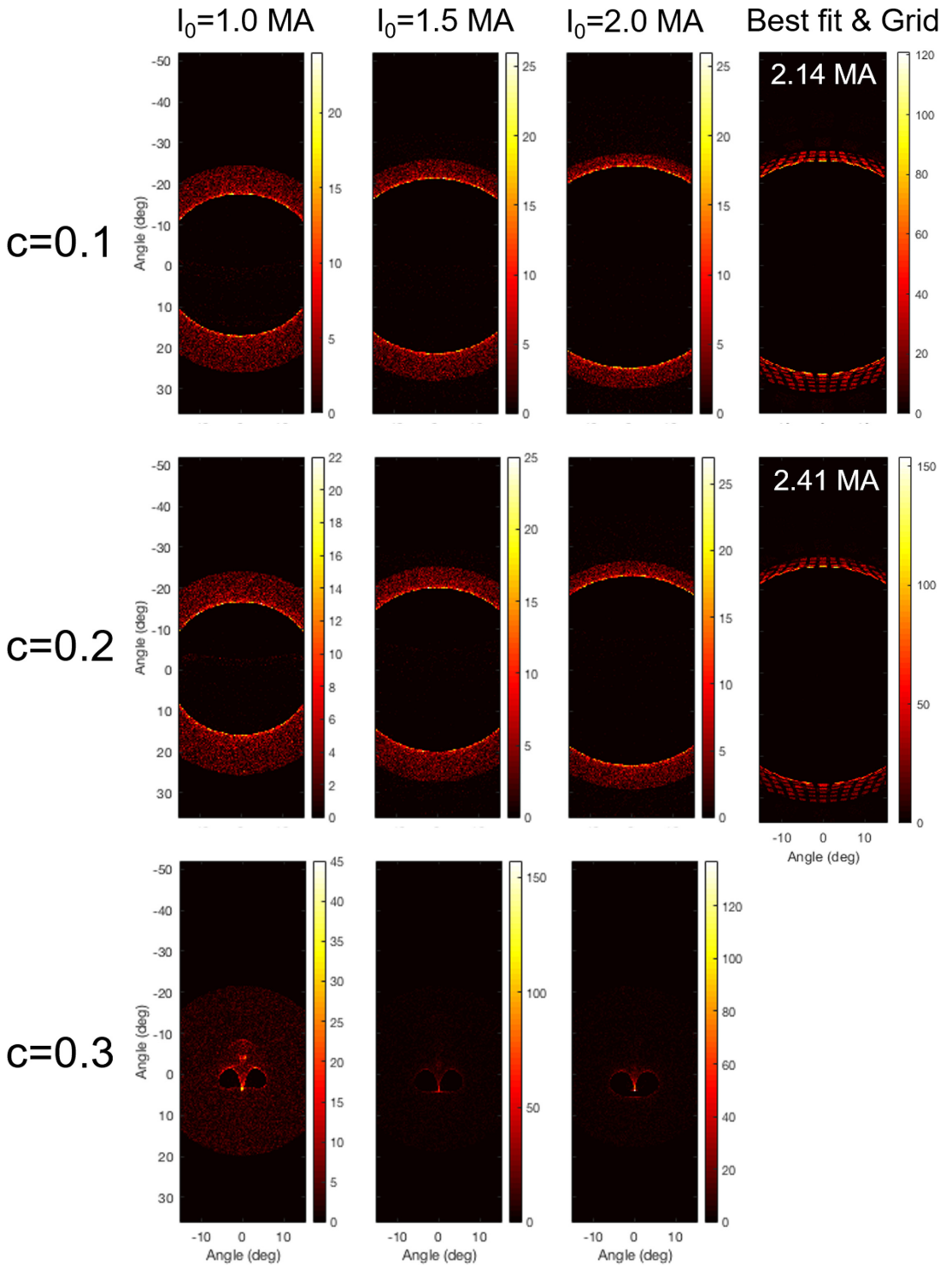

FIG. 9. Some examples of the synthetic proton patterns during the parameter scan. Within the range $0.1 < c < 0.2$ the size of the void scales with the value I_0. For example, when $c = 0.3$ the void will no longer be reproduced for any value of I_0. Also, synthetic proton patterns for the best fit when $c = 0.1, 0.2$ are shown in the rightmost column. The effect of the metal grid in experiment was also applied to the best fit proton pattern.

outflow measurement will be presented, which is the signature of magnetic reconnection. For reference, the magnetic field profile on the x-y plane at $z = 0$ with $c = 0.2$ is shown in Fig. 11.

During the proton deflectometry shots, a low-energy (about 1 J in 1 ns), low-intensity (about 10^{11} W/cm^2) laser pulse was irradiated on the outer surface of the microcoil. By this small heating, the plasma density gradient is significantly decreased and the proton acceleration from the microcoil outer surface, via target normal sheath acceleration (TNSA) mechanism, was eliminated during the irradiation by the main beam.

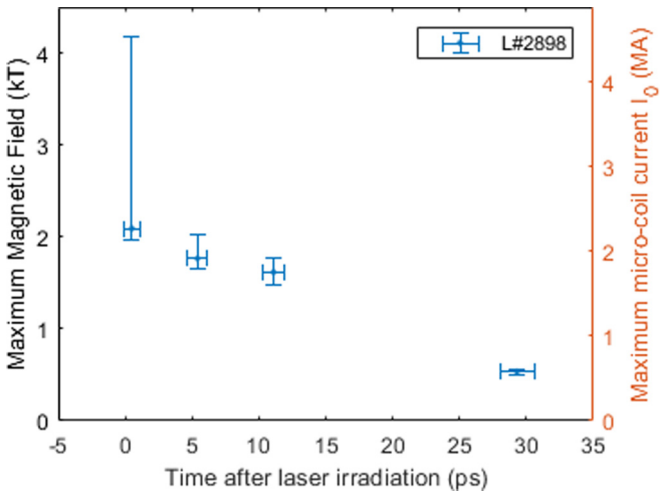

FIG. 10. Temporal evolution of microcoil maximum magnetic field measured in the experiment. Vertical axis represents the maximum magnetic field in the estimated magnetic field map, as well as the value of I_0 in our magnetic field model. The data points correspond to both ordinate axes because the two quantities are directly related.

IV. RECONNECTION OUTFLOW JETS

The accelerated energetic particles formed the magnetic reconnection outflow jets, being measured in our experiment in terms of angular distribution and energy distribution. Angular distribution of the outflow jets is measured by a pair of additional RCF stacks. From two ends of the microcoil along the axial direction, the additional RCF stacks detected a pair of symmetric proton jets with a maximum KE of 6.7 MeV, as shown in Fig. 3. These were interpreted as typical magnetic reconnection outflows. In this experiment, the source of hydrogen atoms for such a proton jet was a contamination layer with a thickness of nanometers that formed on the surface of the microcoil, which is a common feature in laser experiments [24]. During the laser shots of the results presented in this section, the backlighter for magnetic field characterization was not irradiated. This is to eliminate the possibility of contamination by any protons accelerated from backlighter.

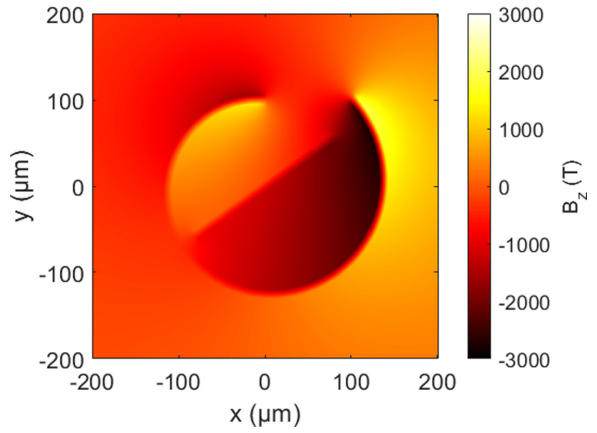

FIG. 11. Cross section of an example of B-field map with $c = 0.2$, produced by the magnetic field model used in our Monte Carlo simulation analysis.

Similar laser shots were performed with shorter microcoils ($l = 100$ μm). Proton jet was observed also in these shots along the axial direction with a significantly larger maximum KE of 19.6 MeV. In the shorter microcoil, our 3D PIC simulations showed that the global magnetic field amplitude did not change significantly, while the shorter microcoil gives a narrower current j_n, which is the dominating constraint of the magnetic field geometry around the magnetic null point. The narrow current reduces the current sheet thickness, leads to enhancement of the magnetic reconnection rate, the reconnection electric field, and thus an increase in jet particles' energy.

The most important result in this study is the energy distribution obtained in this experiment, showing power-law energy distributions with different slope steepness of both protons and electrons. The proton energy distribution was measured with TPS, whose lower limit of detectable KE was 6 MeV as shown in Fig. 12(a). The maximum KE obtained with TPS was 18.8 MeV, which is consistent with the above RCF stack measurement. The proton distribution can be well fitted with a power-law curve $N(E) = N_0 E^{-p_i}$, with the slope index of protons $p_i = 3.013$.

Similarly, the outflow electron KE distribution was measured with ESM as shown in Fig. 12(b). Both thermal and nonthermal components were observed in the electron energy distribution. The best fit with a simple power-law relation gives slope index $p_e = 1.535$, which is a harder distribution than that of the protons. The fitting curve deviates from the experimental one in the range of $E > 2$ MeV, where a superexponential cutoff should be considered as the result of finite spatial scale of this experiment. With including the cutoff, the electron energy distribution is fitted in the form $N(E) = N_0 E^{-p_e} \exp(-E^2/E_c^2)$, similar to the form modeled in Ref. [25] that well explained the small system cases. Here, the system size L is defined as small when L is much shorter than $40\sigma_e\rho_0 \approx 3$ mm, here σ_e and $\rho_0 \equiv m_e c^2/eB_0$ are magnetization and the electron Larmor radius, respectively. The best fit with this cutoff is plotted in Fig. 12(b), with $p_e = 1.215$, $E_c = 1.742$. The cutoff energy is limited by L as $\gamma_e = 0.1L/\rho_0$ in such small system, instead of being limited by secondary tearing instability in large systems.

V. PIC SIMULATION

A. Details of simulation parameters

Numerical simulations of the laser-plasma interaction and its resulting electromagnetic field and particle kinetics were performed by a three-dimensional particle-in-cell (PIC) simulation code EPOCH [26]. In these simulations, plasma representing the microcoil is initially configured by the target shape analytically defined by [13] $r(\theta) = r_0[1 + (\delta r/r_0)(\theta/2\pi)]$.

Limited by our available computational resources, the target size in our simulation is $\frac{1}{30}$ of the real target in all dimensions, $r_0 = 3$ μm and $\delta r = 2$ μm. Moreover, collision effects are not included in this simulation. The simulation box, in size of $12 \times 12 \times 50$ μm, corresponds to $300 \times 300 \times 1250$ cells in Cartesian coordinates, with the simulation cell size $\delta x = 40$ nm and a single time step is 0.059 fs. This cell size

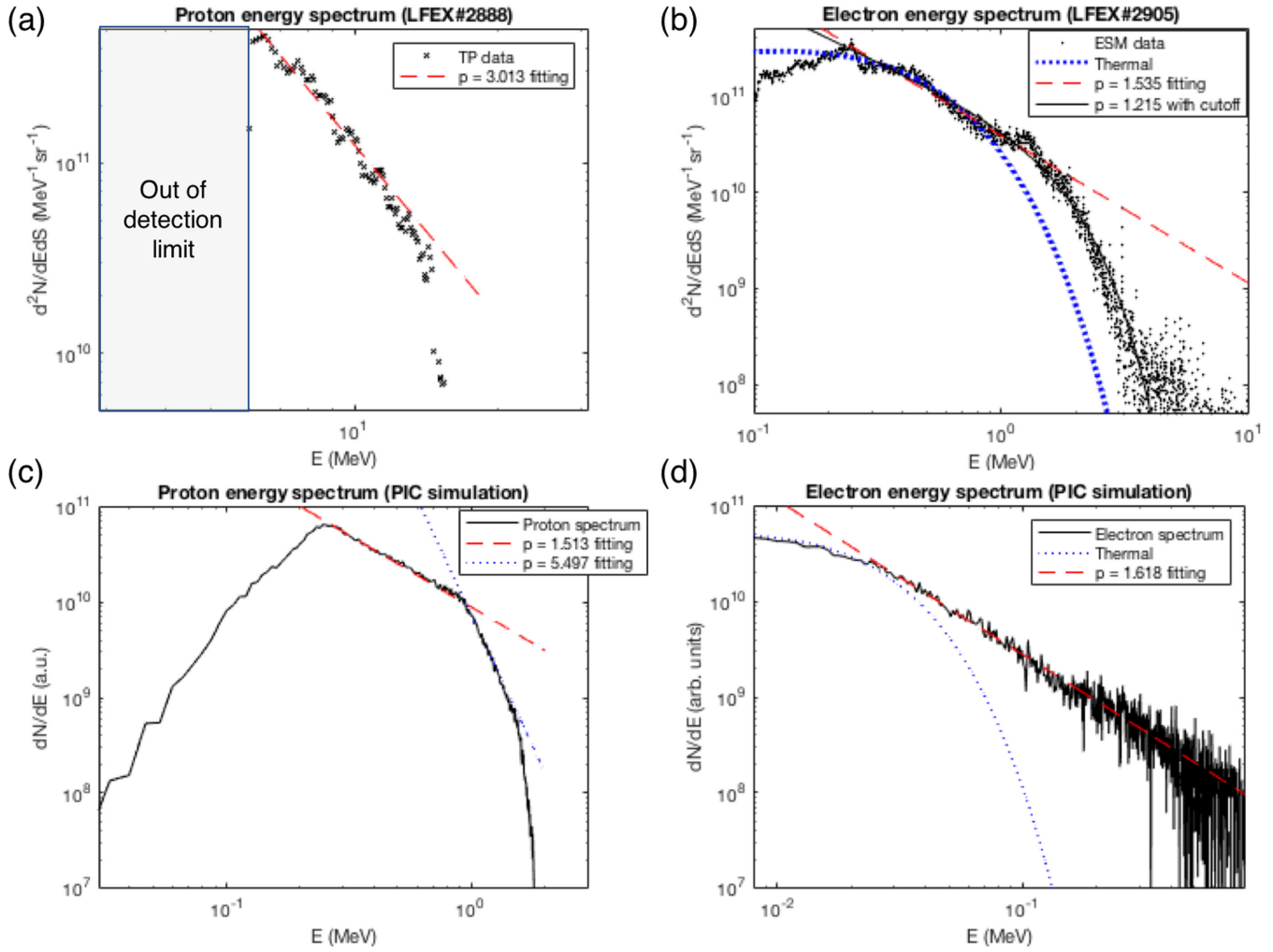

FIG. 12. Proton and electron energy distributions in (a), (b) experiment ($l = 100\ \mu$m) and (c), (d) PIC simulations ($l = 3.3\ \mu$m). (a) The proton energy distribution in KE >6 MeV was measured with Thomson parabola spectrometer (black crosses). The distribution is fitted with the power-law curve whose slope index is $p_i = 3.013$ (blue dotted line). (b) The electron energy distribution was measured with ESM for $E > 100$ keV (black dots). Both thermal and nonthermal components are observed. There are the Maxwell distribution curve (blue dotted line), power-law curve (red dashed line) with slope $p_e = 1.535$, and power-law fitting with superexponential cutoff ($p_e = 1.215$, $E_c = 1.742$) (black solid line) in this graph. (c), (d) Plot energy distributions of (c) protons and (d) electrons escaped from the simulation box in the outflow direction. Both thermal and nonthermal components were observed in the electron energy distribution as the experimental result.

is sufficient to resolve the electron and ion collisionless skin depths (c/ω_{pe} and c/ω_{pi}), estimated as 120 nm and 5 μm, under the maximum electron and ion density $n_e = n_i = 2 \times 10^{27}$ m^{-3} obtained near the magnetic reconnection site in simulation. The coordinate system is defined as follows. The cross section of the microcoil is on the x-y plane, with the x axis parallel to the incident laser propagation direction, and the y axis parallel to its polarization. The z axis is the axial direction of the microcoil, as well as the main direction of the reconnection magnetic field. The microcoil cross-section density profile is shown in Fig. 13. In addition, $r(\theta)$ is defined in polar coordinates with the origin set at $x = y = 5.5\ \mu$m, where $\theta = 0$ is in the $+y$ direction, and θ increases in the anticlockwise direction.

In simulation, the target consists of two layers: an outer layer representing the bulk of the microcoil, and an inner layer representing the preplasma generated by the nanosecond-order prepulse before the arrival of the main pulse. The outer

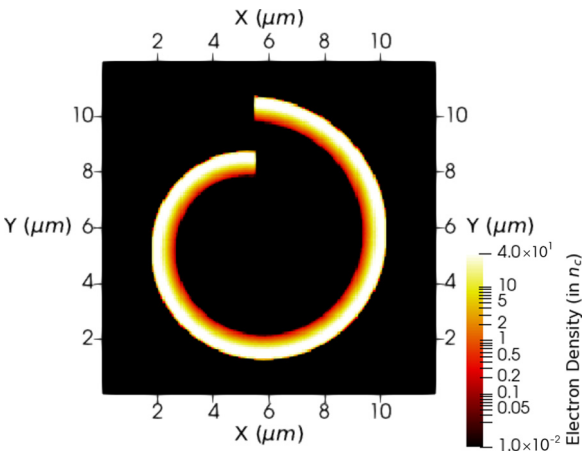

FIG. 13. Initial electron density profile of PIC simulation plotted on the x-y plane.

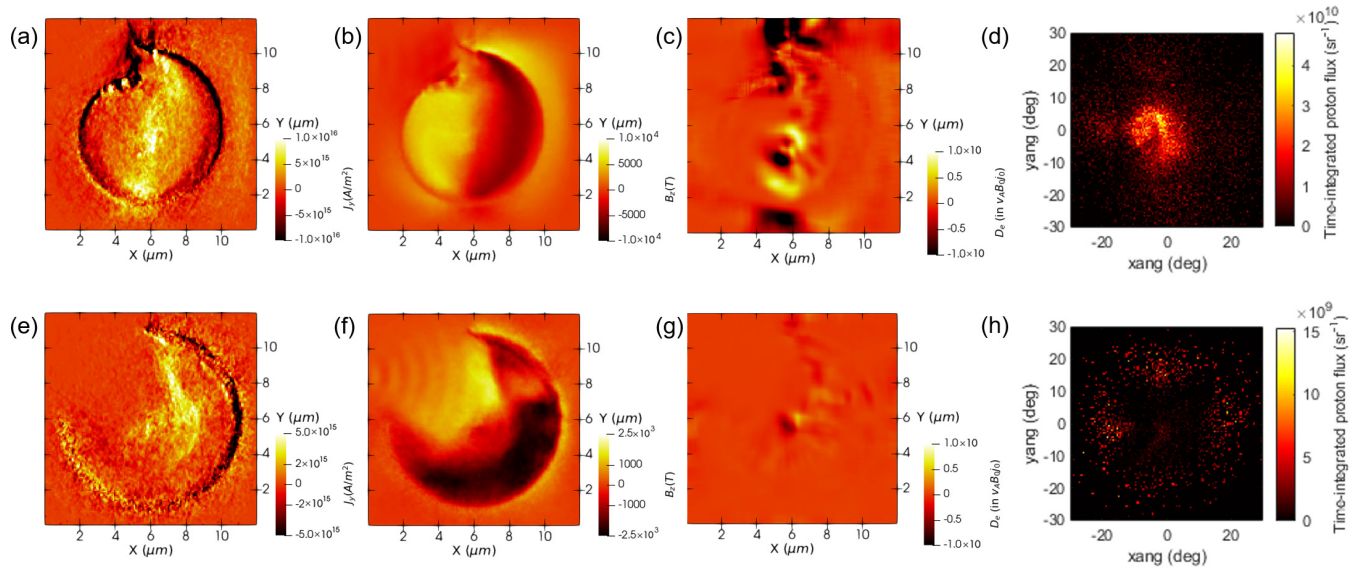

FIG. 14. Results for the (a)–(d) microcoil and (e)–(h) open-cylinder cases. (a), (e) Current density J_y at $z = 0$. An intense $-y$ component on two sides was observed for the microcoil case, indicating bidirectional current generation. For the open-cylinder case, reversal of the sign of the y component was observed at the lower end, and bidirectional current was not generated. (b), (f) Magnetic field B_z at $z = 0$. Here, B_z in opposite directions is observed in both cases, despite the difference in current generation. (c), (g) Dissipation measure D_e at $z = 0$, normalized by $v_{A0}B_0j_0$, with $v_{A0} = 0.023c$, $B_0 = 10^4$ T, and $j_0 = 10^{16}$ A/m^2 the typical values of Alfvén velocity, magnetic field, and current density, respectively. Efficient energy transfer from the electromagnetic field to plasmas was observed only in the microcoil case, where bidirectional B_z was generated by the initial bidirectional current and then reconnected. (d), (h) Reconnection outflow proton angular distribution. The momentum vector direction distribution of the proton that escaped from the simulation box across the $-z$ boundary is plotted, while the $+z$ side showed similar results. All protons with KE >400 keV are integrated, and the origin of the plot indicates the direction parallel to the z axis. The outflow proton beam is only observed in the microcoil case, as a consequence of magnetic reconnection.

surface consists of fully ionized copper plasma with an ion density of $n_i = 1.5 \times 10^{21}$ cm^{-3}, one ion, and 29 electrons per cell. The inner layer consists of proton plasma with an exponential density profile of $n_i = n_e = 40n_c e^{-d/\tau}$, where $n_c = 1.01 \times 10^{21}$ cm^{-3} is the electron critical density, d represents the distance from the outer layer, and $\tau = 0.1$ μm. In the proton plasma, five protons and five electrons are placed per cell. Real ion-electron mass ratio is used in this simulation. This density profile is uniform along the z direction, with a finite length of from 3.3 to 16.7 μm, representing different types of microcoils in the experiment.

In the simulation, the incident laser entered the simulation box from the $-x$ side boundary. For the maximum laser intensity, $I_0 = 1.0 \times 10^{19}$ W/cm^2 at a wavelength of $\lambda_0 = 1.05$ μm, a FWHM of the Gaussian intensity distribution of 1.33 μm, a temporal Gaussian pulse at FWHM of 1.2 ps, and a peak intensity at $t = 0.75$ ps. Polarization of the incident laser is p polarization, the same as in the experiment. In order to separate out the incident laser field, electromagnetic field snapshots are averaged for a single laser period.

B. Verification of magnetic reconnection occurrence in the microcoil

From the three-dimensional PIC simulation, we found that laser irradiation of both ends of the microcoil is the condition for bidirectional current generation, which initiated magnetic reconnection inside the microcoil in our experiment. We performed PIC simulations for two different cases. Case 1 (microcoil case) is identical to the simulation already mentioned above, which is the case with magnetic reconnection. Case 2 (open-cylinder case) is a control simulation intended to produce a case without magnetic reconnection. The initial plasma geometry is modified to an open cylinder, which is three-quarters of a cylinder, so that laser irradiation of the lower end is significantly reduced. The important simulation results are shown in Fig. 14. In these simulations, the emergence of the magnetic reconnection was traced using dissipation measure $D_e = \gamma_e[\boldsymbol{j} \cdot (\boldsymbol{E} + \boldsymbol{v}_e \times \boldsymbol{B}) - \rho_c(\boldsymbol{v}_e \cdot \boldsymbol{E}))]$, where γ_e is the Lorentz factor of bulk electrons, $\boldsymbol{j}$ the current density, $\boldsymbol{E}$ and $\boldsymbol{B}$ the local electric and magnetic fields, $\boldsymbol{v}_e$ the average velocity of electrons, and ρ_c the charge density. This dissipation measure is a Lorentz-invariant scalar quantity of the energy transfer from the electromagnetic field to the plasma in the rest frame of the electron [27], which is validated in laser-produced plasmas [28]. Magnetic reconnection sites are correlated to the observation of proton jets and bidirectional currents [Figs. 14(c) and 14(d)], but not in cases where neither proton jets nor bidirectional currents are generated as shown in Figs. 14(g) and 14(h). The contour line of $D_e = 0.5v_{A0}B_0j_0$ is indicated in Fig. 1(b), which is consistent with the expected site for the magnetic reconnection. The reconnection current sheet thickness, electron diffusion region thickness, and aspect ratio are 1.8 μm, 0.5 μm, and 14, respectively, in the PIC simulations. Also, no significant guide field component was observed in the simulation.

Based on these results, we observed that bidirectional current is generated only in the microcoil case, where laser irradiated both ends of the cylinder. As a result, dissipation from the electromagnetic field to the plasma is much more

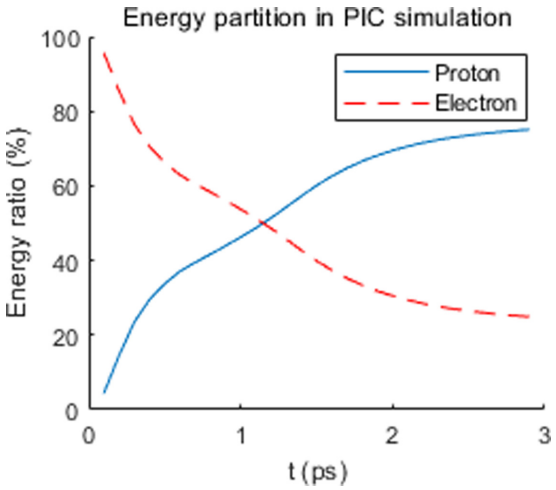

FIG. 15. Energy partition between proton and electrons. The contributions of electron and proton on the total particle kinetic energy are shown.

efficient in the microcoil case, even though antiparallel B_z is observed in both cases. Outflow proton jets, as shown in Figs. 14(d) and 14(h), are observed only in the microcoil case, in which magnetic reconnection occurs.

C. Energetics of accelerated particles

Synthetic energy distributions of particles escaped from PIC simulation box along the jet direction are plotted in Figs. 12(c) and 12(d), reproducing the experimental observed steeper proton energy distributions slope, in the range of proton KE comparable to the maximum electron KE. The cutoff particle energy in the simulation is one order lower than the experimental one, as the consequence of smaller system spatial scale L in the 3D PIC simulation that is 30 times smaller than the experiment. Similar dependency was confirmed in previous study by 2D PIC simulation on both electron-proton plasma [29] and pair plasmas [25,30].

In astrophysics, understanding the energy balance during energy conversion process is important, especially when the contribution of one species is the dominating energy source. Therefore, the energy partition between electrons and ions in magnetic reconnection is in great interest. By this reason, the energy partition of magnetic reconnection scheme in this work are measured from the simulation. We estimated the energy partition by two different approaches, accounts background and outflow particles, respectively, in terms of [31]. The energy partition between background protons and electrons is estimated from the total particle kinetic energy integrated through the whole simulation. The time evolution of the energy partition is shown in Fig. 15. During the laser irradiation, ion contribution rapidly increases from zero to 60%. After the laser irradiation, the ratio gradually increased and approaches 75% at the end of the simulation. The energy partition between outflow protons and electrons is estimated from the particles escaped from the simulation. The kinetic energy of escaped particles was integrated to make a comparison between species. Only particles moving in angle $<60^\circ$ from outflow direction were counted to exclude particles directly accelerated by the laser field. Counting all escaped particles until $t = 2.9$ ps, the ion contribution was 71.2%. To conclude, both approaches showed ion contribution of between 70% and 80% within the total particle energy. This value is slightly higher than the results in [31] and [29], 67% and ~70%, respectively, for the semirelativistic case. The different ion-electron mass ratio between different simulations may contribute to this difference. On the other hand, experimental study on the energy partition in this magnetic reconnection scheme is practically challenging, but worth to perform in the future.

VI. DISCUSSIONS AND CONCLUSIONS

In this experiment, a highly magnetized relativistic plasma structure with a reconnection layer was produced as a compact object. The outflow spectra were measured to have a hard component, consistent with 3D PIC simulations with similar plasma parameters. We observed the difference between the slopes of proton and electron ($p_e < p_i$) in the particle energy distributions. This is the consequence of higher electron magnetization than the proton one, which supports the results of Melzani's study about the repartition between electrons and ions [31]. Here, we estimated the inflow proton and electron magnetization, which is defined as the ratio of energy flux in the reconnecting magnetic field to the energy flux of particles, $\sigma_s = B_0^2/(\mu_0 n_s m_s c^2 \gamma_s h_{0,s})$, for particle species s, where n_s is the number density of species, m_s the particle mass, $\gamma_s = (1 - v_s^2/c^2)^{-1/2}$ the Lorentz factor, and $h_{0,s} \simeq 1 + (5/2)(T/mc^2)$ the enthalpy [32]. A two-dimensional, real-scale PIC simulation was performed to estimate the physical quantities n_s and $\gamma_s h_{0,s}$, where the density profile of the proton plasma layer is set to match the nanometer-scale solid density layer identified in the previous study [24] in terms of areal density. After accounting for the downscaling of PIC simulation from real situation, parameters ranged between $n_i = n_e = 10^{23}$–10^{24} m^{-3}, $\gamma_e h_{0,e} = 1.5$–10, and $\gamma_i h_{0,p} \simeq 1$. Based on the experimental result of $B_0 = 2.1$ kT, we obtained $\sigma_e = 20$–100 and $\sigma_i = 0.05$–0.5. In this range of electron magnetization σ_e, a hard electron energy distribution is expected to be generated through first-order Fermi acceleration [33] and direct acceleration by reconnection electric fields [31]. In contrast to the electron, the slope of proton energy distribution is much steeper because of less proton magnetization $\sigma_i < 1$. These features agree with Melzani's result [31].

A. Other particle acceleration mechanisms from microcoil

It is important to guarantee that the energetic particles detected along the outflow direction are accelerated by magnetic reconnection, instead of other mechanisms during laser-plasma interaction. In Sec. V, we have showed the observation of outflow jets is directly related to the existence of magnetic reconnection by numerical simulations. Here, we provide additional discussions to rule out the possibility that the energetic particles may be accelerated by other mechanisms.

The candidate that is most likely to accelerate protons to over 10 MeV inside the microcoil, under the current experimental situation, is the "backward emission" during the target normal sheath acceleration [34]. The LFEX laser fulfilled both

TABLE I. Physical parameters in various environments, including this laboratory plasma and some typical astronomical objects. The relativistic Alfvén velocity $v_A/c = [\sigma_{i+e}/(1+\sigma_{i+e})]^{-1/2}$ is also shown.

Magnetic reconnection plasma	B_0 (T)	n_e (m^{-3})	ω_{pe} (rad/s)	T_e (K)	σ_e	v_A/c
Laser-driven microcoil	2.1×10^3	10^{23}–10^{24}	$\sim 2 \times 10^{13}$	10^9–10^{10}	20–100	0.22–0.58
Cygnus X-1 [35]	10^3	5×10^{24}	10^{14}	10^9	130	0.3
Microquasar coronae [31,36]	10^1–10^3	10^{19}–10^{22}	10^{11}–10^{13}	10^9	10^{-1}–10^5	0.003–1
GRB jet [31,37]	7×10^4	10^{16}	5×10^9	10^8	5×10^{12}	0.9

high laser intensity ($>10^{18}$ W/cm^2) and high laser contrast (at least, $>10^6$), the requirement for this process to occur. However, ions accelerated by this mechanism are highly anisotropic, with momentum distribution localized around the target normal direction (in terms of the PIC simulation coordinates, a direction on the x-y plane). Under this magnetic field which diminishes in a distance well before the particles are detected, such a proton population could not be collimated in the outflow direction ($\pm z$ direction) by a global magnetic field directed in the $\pm z$ direction.

The remaining possibility is particle acceleration from the microcoil itself, initially traveling to the outflow direction ($\pm z$ direction). Although we did not observe such protons from our simulation, we experimentally inspected such possibility by performing a measurement on the sideway accelerated proton, during irradiation of a thin foil of size 300×300 μm, which is comparable to the size of the microcoil. The maximum energy of the sideway accelerated proton is much lower than the TNSA accelerated proton detected in the same laser shot, in a factor of 3. Such maximum energy cannot explain the outflow observed in the magnetic reconnection experiment, and could be excluded as the possible source of the observed outflow protons.

B. Application on astrophysics

Our experimental test of hard electron energy distribution from semirelativistic magnetic reconnection gives insight into high-energy astrophysics. Table I shows physical parameters in various environments, including this laser experiment and some typical astronomical objects, including Cygnus X-1, a well-known example of a galactic x-ray source. For Cygnus X-1, the values of the analytical model [35] were set to $B_0 = 10^3$ T, $n_e = n_i = 5 \times 10^{22}$ m^{-3}, $\gamma_e h_{0,e} = 1.5$, and an electron magnetization of $\sigma_e = 130$. Recently, a jet model was proposed as a candidate mechanism of x-ray emission that can account for recent observations of Cygnus X-1, in which hard electron energy distributions $p_e = 1.4$–1.5 are formed in the jets by efficient particle acceleration [5]. We experimentally showed such a hard electron population can be built in the magnetic reconnection outflow jet, under inflow electron magnetization $\sigma_e = 20$–100, which is similar to the electron magnetization of galactic x-ray source Cygnus X-1 as shown in Table I. According to recent simulation results [31], the power-law slope of accelerated electron depends mainly on σ_e and v_A, independent of other parameters including simulation spatial scale or time duration. Based on these previous investigations, our result provides evidence from the experimental side, for the possibility of hard electron energy distribution formation in Cygnus X-1 through magnetic reconnection.

C. Conclusions

In conclusion, we performed a magnetic reconnection experiment in laser laboratory using a microcoil scheme, and demonstrated the hard power-law electron energy distribution from semirelativistic magnetic reconnection regime, with the reconnection magnetic field measured as 2.1 kT. In contrast to the previous studies of astrophysical phenomena with laboratory plasmas, most of the major plasma parameters in our experiment are directly comparable to astronomical plasma, for example, Cygnus X-1 accretion disk corona, without applying MHD scaling laws. The main differences between the laboratory and astronomical plasmas are the spatial and temporal scales, which are reflected in the difference of cutoff electron energy $\gamma_e mc^2$ when we compare our experiment result and Cygnus X-1 emission model [5] as example: $\gamma_e \sim 20$ was detected in our experiment in a system of 100 μm (10^{-4} m), while cutoff $\gamma_e \sim 10^4$ was modeled in Cygnus X-1, with spatial scale of accretion disk corona which should be comparable to the gravitational radius $\sim 5 \times 10^4$ m. In this case, the spatial scale of a possible magnetic reconnection region in astronomical objects may be further estimated, based on further laboratory studies performed with a parameter scan on spatial scales of the reconnection region.

ACKNOWLEDGMENTS

The authors thank the technical staff of Institute of Laser Engineering (ILE) and the Cyber Media Center at Osaka University for their support on laser operation, target fabrication, plasma diagnostics, and computer simulation. We appreciate valuable discussions with T. Sano, F. Guo, and D. Uzdensky on MHD phenomena occurring in an accretion disk, particle acceleration mechanism in magnetic reconnection, and semirelativistic magnetic reconnection in electron-ion plasma respectively. We thank J. Zhong and his staff and students for discussions during the experiment. This work was supported by fundings from ILE (2017A1-KORNEEV), JSPS by Grant-in-Aid for JSPS Research Fellow (Grants No. 18J11119 and No. 18J11354), Grants-in-Aid, KAKENHI (Grants No. 15KK0163, No. 15K21767, No. 16K13918, and No. 16H02245), and Bilateral Program for Supporting International Joint Research, MEPhI by Academic Excellence Project (Contract No. 02.a03.21.0005-27.08.2013), Ministry of Science and Higher Education of the Russian Federation (Project No. FSWU-2020-0035), and Matsuo Research Foundation. This work was also partially supported by PRESTO (JPMJPR15PD) commissioned by JST. M.E., E.d'H. and J.J.S. were supported by Investments for the future program

IdEx Bordeaux LAPHIA (ANR-10-IDEX-03-02) and by the EUROfusion Consortium and have received funding from the Euratom research and training programme 2014–2018 under Grant Agreement No. 633053. The views and opinions expressed herein do not necessarily reflect those of the European Commission.

[1] M. Yamada, R. Kulsrud, and H. Ji, Magnetic reconnection, Rev. Mod. Phys. **82**, 603 (2010).

[2] P. A. Sweet, 14. The neutral point theory of solar flares, *Symposium-International Astronomical Union* (Cambridge University Press, Cambridge, 1958), Vol. 6, pp. 123–134.

[3] W. J. Hughes, The magnetopause, magnetotail, and magnetic reconnection, in *Introduction to Space Physics*, edited by M. G. Kivelson and C. T. Russell (Cambridge University Press, New York, 1995), Chap. 9, p. 227.

[4] T. Di Matteo, Magnetic reconnection: flares and coronal heating in active galactic nuclei, Mon. Not. R. Astron. Soc. **299**, L15 (1998).

[5] A. A. Zdziarski, P. Pjanka, M. Sikora, and Ł. Stawarz, Jet contributions to the broad-band spectrum of Cyg X-1 in the hard state, Mon. Not. R. Astron. Soc. **442**, 3243 (2014).

[6] Y. Ono, M. Yamada, T. Akao, T. Tajima, and R. Matsumoto, Ion Acceleration and Direct Ion Heating in Three-Component Magnetic Reconnection, Phys. Rev. Lett. **76**, 3328 (1996).

[7] M. Yamada, H. Ji, S. Hsu, T. Carter, R. Kulsrud, N. Bretz, F. Jobes, Y. Ono, and F. Perkins, Study of driven magnetic reconnection in a laboratory plasma, Phys. Plasmas **4**, 1936 (1997).

[8] J. Egedal, W. Fox, N. Katz, M. Porkolab, K. Reim, and E. Zhang, Laboratory Observations of Spontaneous Magnetic Reconnection, Phys. Rev. Lett. **98**, 015003 (2007).

[9] J. Olson, J. Egedal, S. Greess, R. Myers, M. Clark, D. Endrizzi, K. Flanagan, J. Milhone, E. Peterson, J. Wallace *et al.*, Experimental Demonstration of the Collisionless Plasmoid Instability Below the Ion Kinetic Scale During Magnetic Reconnection, Phys. Rev. Lett. **116**, 255001 (2016).

[10] J. Zhong, Y. Li, X. Wang, J. Wang, Q. Dong, C. Xiao, S. Wang, X. Liu, L. Zhang, L. An, F. Wang, J. Zhu, Y. Gu, X. He, G. Zhao, and J. Zhang, Modelling loop-top X-ray source and reconnection outflows in solar flares with intense lasers, Nat. Phys. **6**, 984 (2010).

[11] X. X. Pei, J. Y. Zhong, Y. Sakawa, Z. Zhang, K. Zhang, H. G. Wei, Y. T. Li, Y. F. Li, B. J. Zhu, T. Sano, Y. Hara, S. Kondo, S. Fujioka, G. Y. Liang, F. L. Wang, and G. Zhao, Magnetic reconnection driven by Gekko XII lasers with a Helmholtz capacitor-coil target, Phys. Plasmas **23**, 032125 (2016).

[12] A. Raymond, C. Dong, A. McKelvey, C. Zulick, N. Alexander, T. Batson, A. Bhattacharjee, P. Campbell, H. Chen, V. Chvykov *et al.*, Relativistic magnetic reconnection in the laboratory, Phys. Rev. E **98**, 043207 (2018).

[13] P. Korneev, E. d'Humières, and V. Tikhonchuk, Gigagauss-scale quasistatic magnetic field generation in a snail-shaped target, Phys. Rev. E **91**, 043107 (2015).

[14] Y. Abe, K. Law, P. Korneev, S. Fujioka, S. Kojima, S.-H. Lee, S. Sakata, K. Matsuo, A. Oshima, A. Morace *et al.*, Whispering gallery effect in relativistic optics, JETP Lett. **107**, 351 (2018).

[15] T. Nakamura, S. Kato, H. Nagatomo, and K. Mima, Surface-Magnetic-Field and Fast-Electron Current-Layer Formation by Ultraintense Laser Irradiation, Phys. Rev. Lett. **93**, 265002 (2004).

[16] H. Shiraga, S. Fujioka, M. Nakai, T. Watari, H. Nakamura, Y. Arikawa, H. Hosoda, T. Nagai, M. Koga, H. Kikuchi *et al.*, Fast ignition integrated experiments with Gekko and LFEX lasers, Plasma Phys. Controlled Fusion **53**, 124029 (2011).

[17] S. C. Wilks, A. B. Langdon, T. E. Cowan, M. Roth, M. Singh, S. Hatchett, M. H. Key, D. Pennington, A. MacKinnon, and R. A. Snavely, Energetic proton generation in ultra-intense laser–solid interactions, Phys. Plasmas **8**, 542 (2001).

[18] M. Mori, M. Kando, A. S. Pirozhkov, Y. Hayashi, A. Yogo, N. Yoshimura, K. Ogura, M. Nishiuchi, A. Sagisaka, S. Orimo, M. Kado, A. Fukumi, Z. Li, S. Nakamura, A. Noda, and H. Daido, New detection device for Thomson parabola spectrometer for diagnosis of the laser-plasma ion beam, Plasma Fusion Res. **1**, 042 (2006).

[19] C. K. Li, F. H. Séguin, J. A. Frenje, J. R. Rygg, R. D. Petrasso, R. P. J. Town, P. A. Amendt, S. P. Hatchett, O. L. Landen, A. J. Mackinnon, P. K. Patel, V. A. Smalyuk, T. C. Sangster, and J. P. Knauer, Measuring E and B Fields in Laser-Produced Plasmas with Monoenergetic Proton Radiography, Phys. Rev. Lett. **97**, 135003 (2006).

[20] J. Santos, M. Bailly-Grandvaux, L. Giuffrida, P. Forestier-Colleoni, S. Fujioka, Z. Zhang, P. Korneev, R. Bouillaud, S. Dorard, D. Batani *et al.*, Laser-driven platform for generation and characterization of strong quasi-static magnetic fields, New J. Phys. **17**, 083051 (2015).

[21] K. Law, M. Bailly-Grandvaux, A. Morace, S. Sakata, K. Matsuo, S. Kojima, S. Lee, X. Vaisseau, Y. Arikawa, A. Yogo *et al.*, Direct measurement of kilo-tesla level magnetic field generated with laser-driven capacitor-coil target by proton deflectometry, Appl. Phys. Lett. **108**, 091104 (2016).

[22] T. Sato, Y. Iwamoto, S. Hashimoto, T. Ogawa, T. Furuta, S.-i. Abe, T. Kai, P.-E. Tsai, N. Matsuda, H. Iwase *et al.*, Features of particle and heavy ion transport code system (phits) version 3.02, J. Nucl. Sci. Technol. **55**, 684 (2018).

[23] O. Chubar, P. Elleaume, and J. Chavanne, A three-dimensional magnetostatics computer code for insertion devices, J. Synchrotron Radiat. **5**, 481 (1998).

[24] M. Allen, P. K. Patel, A. Mackinnon, D. Price, S. Wilks, and E. Morse, Direct Experimental Evidence of Back-Surface Ion Acceleration from Laser-Irradiated Gold Foils, Phys. Rev. Lett. **93**, 265004 (2004).

[25] G. Werner, D. Uzdensky, B. Cerutti, K. Nalewajko, and M. Begelman, The extent of power-law energy spectra in collisionless relativistic magnetic reconnection in pair plasmas, Astrophys. J. Lett. **816**, L8 (2015).

[26] T. Arber, K. Bennett, C. Brady, A. Lawrence-Douglas, M. Ramsay, N. Sircombe, P. Gillies, R. Evans, H. Schmitz, A. Bell *et al.*, Contemporary particle-in-cell approach to laser-plasma modelling, Plasma Phys. Controlled Fusion **57**, 113001 (2015).

[27] S. Zenitani, M. Hesse, A. Klimas, and M. Kuznetsova, New Measure of the Dissipation Region in Collisionless Magnetic Reconnection, Phys. Rev. Lett. **106**, 195003 (2011).

[28] Z. Xu, B. Qiao, H. X. Chang, W. P. Yao, S. Z. Wu, X. Q. Yan, C. T. Zhou, X. G. Wang, and X. T. He, Characterization of magnetic reconnection in the high-energy-density regime, Phys. Rev. E **93**, 033206 (2016).

[29] G. Werner, D. Uzdensky, M. Begelman, B. Cerutti, and K. Nalewajko, Non-thermal particle acceleration in collisionless relativistic electron–proton reconnection, Mon. Not. R. Astron. Soc. **473**, 4840 (2017).

[30] F. Guo, X. Li, H. Li, W. Daughton, B. Zhang, N. Lloyd-Ronning, Y.-H. Liu, H. Zhang, and W. Deng, Efficient production of high-energy nonthermal particles during magnetic reconnection in a magnetically dominated ion–electron plasma, Astrophys. J. Lett. **818**, L9 (2016).

[31] M. Melzani, R. Walder, D. Folini, C. Winisdoerffer, and J. M. Favre, The energetics of relativistic magnetic reconnection: ion-electron repartition and particle distribution hardness, Astron. Astrophys. **570**, A112 (2014).

[32] M. Melzani, C. Winisdoerffer, R. Walder, D. Folini, J. M. Favre, S. Krastanov, and P. Messmer, Apar-T: code, validation, and physical interpretation of particle-in-cell results, Astron. Astrophys. **558**, A133 (2013).

[33] F. Guo, Y.-H. Liu, W. Daughton, and H. Li, Particle acceleration and plasma dynamics during magnetic reconnection in the magnetically dominated regime, Astrophys. J. **806**, 167 (2015).

[34] T. Ceccotti, A. Lévy, H. Popescu, F. Réau, P. D. Oliveira, P. Monot, J. P. Geindre, E. Lefebvre, and P. Martin, Proton Acceleration with High-Intensity Ultrahigh-Contrast Laser Pulses, Phys. Rev. Lett. **99**, 185002 (2007).

[35] M. Del Santo, J. Malzac, R. Belmont, L. Bouchet, and G. De Cesare, The magnetic field in the x-ray corona of Cygnus X-1, Mon. Not. R. Astron. Soc. **430**, 209 (2013).

[36] R. Reis and J. Miller, On the size and location of the x-ray emitting coronae around black holes, Astrophys. J. Lett. **769**, L7 (2013).

[37] J. C. McKinney and D. A. Uzdensky, A reconnection switch to trigger gamma-ray burst jet dissipation, Mon. Not. R. Astron. Soc. **419**, 573 (2011).